

Research Article

Disturbance Elimination for the Modular Joint Torque Sensor of a Collaborative Robot

He Zhang , Wenlei Qin, Yongsheng Gao , Qiang Li, Zhigang Chen, and Jie Zhao 

State Key Laboratory of Robotics and System, Harbin Institute of Technology, Harbin 150080, China

Correspondence should be addressed to He Zhang; zhanghe0451@hit.edu.cn and Yongsheng Gao; gaoy@s@hit.edu.cn

Received 19 May 2020; Revised 31 July 2020; Accepted 1 August 2020; Published 20 October 2020

Guest Editor: Carlos Llopis-Albert

Copyright © 2020 He Zhang et al. This is an open access article distributed under the Creative Commons Attribution License, which permits unrestricted use, distribution, and reproduction in any medium, provided the original work is properly cited.

The ability to obtain accurate torque information and detect collision information is the key demand for collaborative robots. Given the highly integrated modular joint, the joint torque-sensing system is disturbed by other elements during online measurement, affecting the accuracy of measurement. For example, the torque ripple caused by the periodic deformation of the flexspline of the harmonic driver and the temperature drift due to the heating of motor are the two main factors affecting the measurement of the torque sensor. In this study, a torque sensor suitable for a modular joint is developed. Moreover, a strain gauge configuration based on a specified phase difference for torque ripple cancelation and a temperature compensation method based on the combination of the Wheatstone bridge and a nonlinear model are proposed. Finally, the performance of the developed sensor is experimentally evaluated.

1. Introduction

Collaborative robots can be remarkably applied in various industries, for example, medical treatment, 3C electronics, and public service [1, 2]. To avoid injury from robots, the collision detection technology of robots has attracted extensive attention. This technology based on a visual sensor needs to collect and process a high volume of real-time data [3]. Collision detection based on a motor current should predict interference and assembly error model to accurately estimate torque [4]. To resolve these problems, many scholars have embedded a joint torque sensor into robot joints [5, 6]. In addition, the method based on strain gauges to measure force or moment is more mature and reliable, and this method is favored by researchers [7, 8].

At present, the harmonic drive is widely used in collaborative robots because of its high gear-reduction ratio and high torque ability in a compact geometry. During the operation of the harmonic driver, the elliptical wave generator facilitates the periodic deformation of the flexspline. This process couples the output of the torque sensor embedded in the robot joint with the periodic noise, which is also known as torque ripple [9]. Taghirad designed a Kalman

filter to compensate for the torque ripple [10]. However, this method needs to estimate the model of the torque ripple in advance. Jung adopted the order tracking method based on resampling to eliminate the torque ripple [11]. However, the resampling method is only applicable when the position changes. Considering that the torque ripple mainly originates from the deformation of the flexspline, Hashimoto balanced the torque ripple by pasting strain gauges on the flexspline and forming the Wheatstone bridge [12]. This method avoids numerous calculations and improves response speed, but strain gauges should be pasted on the bottom of the flexspline in a certain configuration. In addition, the torsional stiffness of the flexspline should also be known. To reduce the placement error of the strain gauges and torque ripple, an elastomer with mutually perpendicular spokes and pasted strain gauges has been designed by adding two signals from two sets of strain gauges to eliminate the torque ripple [13, 14]. However, this method needs two sets of signal conditioning circuits.

During operation of the robot, the heat generated by the motor is easily transmitted to the torque sensor through the metal transmission shaft and metal flange. This process creates a temperature drift in the output signal of the torque

sensor. The Wheatstone bridge is commonly used in the joint torque measurement with strain gauge [12, 15]. However, when strain gauges are heated unevenly, this technique deteriorates the sensing performance. Francisco studied the temperature drift of a six-axis force torque sensor based on the strain gauge by assuming that the temperature drift of this sensor has a linear relationship with six-axis force. In this study, the calibration matrix and temperature drift coefficient of the sensor are estimated simultaneously using linear regression based on the least square method [16]. Sun modeled the temperature drift of a six-axis force torque sensor of a space manipulator by using the least square support vector machine and particle swarm optimization algorithm to optimize the parameters of the model [17]. However, the software compensation depends on the accuracy of the model. Moreover, the more accurate the model is, the more the calculation needed is, and this process introduces transmission delay. Therefore, to balance the accuracy and delay of the sensor, hardware and software are combined to compensate for the temperature drift.

In this study, a joint torque sensor embedded in a modular joint, which includes a motor, a harmonic drive, a torque sensor, and an encoder, is proposed to mainly address how a robot obtains accurate torque-sensing ability. The main research contents are as follows. A torque ripple cancelation method, which combines a specially designed elastic body and the Wheatstone bridge in a special form, is proposed. Thus, the periodic disturbance from the harmonic drive can be compensated. In addition, the temperature compensation method based on the combined hardware and software is proposed. Another Wheatstone bridge is distributed symmetrically with respect to the first Wheatstone bridge to cancel the torque ripple. A nonlinear model is also proposed to further reduce the error from the temperature drift.

This paper is organized as follows. The design of the torque sensor and the theoretical analysis of the torque ripple cancelation, temperature compensation, and collision detection are discussed in Section 2. In Section 3, the experimental setups for the developed torque sensor are presented. The evaluation results of the torque ripple cancelation, the temperature drift compensation, and collision detection are addressed in Section 4. Finally, the conclusion is provided in Section 5.

2. Proposed Approach

2.1. Problem Statement. A collaborative robot is a robot that can directly and physically interact with a human operator in a shared workspace. For example, a collaborative robot with surgery tool and several doctors perform an eye or orthopedic surgery together. For safety requirements, one of the most basic characteristics of a collaborative robot is the estimation of external force or collision detection. Industrial robots measure the external force by using a six-axis force torque sensor, which is only suitable for a force/torque acting on the robot end-effector. However, a torque sensor arranged on the robot joint can estimate the force acting on most areas of the robot. Therefore, a joint torque sensor is

one of the necessary hardware devices for a collaborative robot. To facilitate repair and reconfiguration, collaborative robots need modular joints, which connect adjacent links and integrate the drive, sensing, and control.

A modular joint unit usually consists of a motor, a harmonic drive, a joint torque sensor, a joint encoder, and other modules. The shaft of the motor is directly connected to the wave generator of the harmonic driver, while the joint torque sensor is connected to the flexspline through the connector. As shown in Figure 1, the periodic deformation of the flexspline propagates to the joint torque sensor through the connector. This process mixes the output of the joint torque sensor with the torque ripple. The motor is the main heat source while the modular joint is used. The heat will be transferred to the joint torque sensor through the harmonic drive and connector, causing the output of the joint torque sensor to drift, even if the external load of the torque sensor is constant. Thus, for accurate collision detection, the design of the sensor should cancel the torque ripple and the temperature drift.

2.2. Design of Joint Torque Sensor. As shown in Figure 2, the elastic body of the sensor is designed as the spoke type; that is, the inner and outer rings are connected by spokes. The slit on the spoke makes the strain of the sensor equivalent to that of the spoke. Given the idle space outside the spoke, a signal processing circuit can be built in this space to make the sensor compact and thinner. In addition, four protective beams are added. When the sensor is overloaded, the protective beam will prevent irreversible damage to the sensor.

Based on the proposed torque sensor design, the finite element method (FEM) is conducted using ANSYS. The maximum sensing torque is 70 Nm, and the maximum load that the torque sensor can endure is set to 180 Nm. The maximum strain is 0.003 mm as calculated from the design of the conditioning circuit. The 6061 aluminum alloy is selected to fabricate the sensor because of its small elastic coefficient and large yield strength. The coordination of the torque sensor is shown in Figure 3. The applied load is $Mx = 180 \text{ Nm}$. The structural parameters of the spoke are calculated by FEM are shown in Table 1. The deformation of the body is illustrated in Figure 4. The analytical results are used to specify the location of the strain gauge.

The mechanical strain of the torque sensor can be measured by using the strain gauge forming the Wheatstone bridge. However, the voltage signal of the Wheatstone bridge is too weak to collect. Hence, the weak electrical signal should be amplified and filtered. The analog signal is further converted into digital form to read the torque signal on the chip. In addition, a temperature-measuring circuit is installed to compensate for the temperature drift. A conditioning circuit board is designed and consists of an ADA4528 amplifier with a factor of 200, an RC low pass filter to cancel the noise signal, and an AD7790 with 16 bit buffered sigma-delta ADC to convert the analog signal to digital signal. The AD7790 transmits the digital signal to a microcontroller STM32F103T8 through the SPI

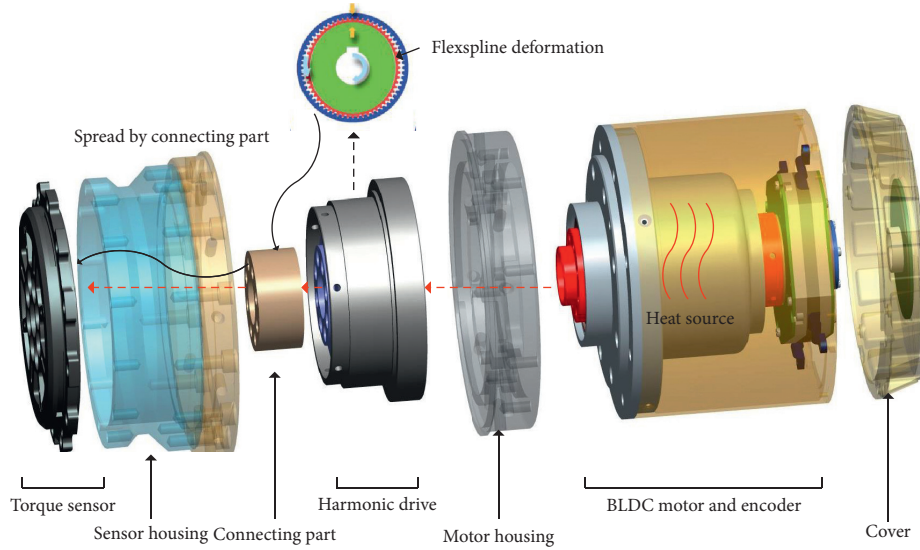


FIGURE 1: Expanded view of the developed modular joint.

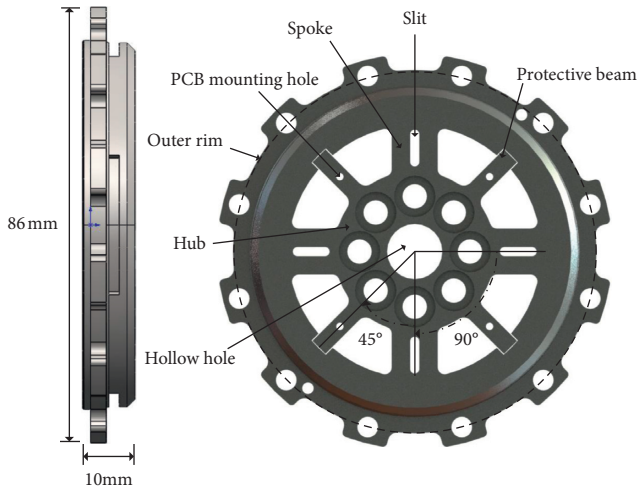


FIGURE 2: Mechanical structure of the sensor.

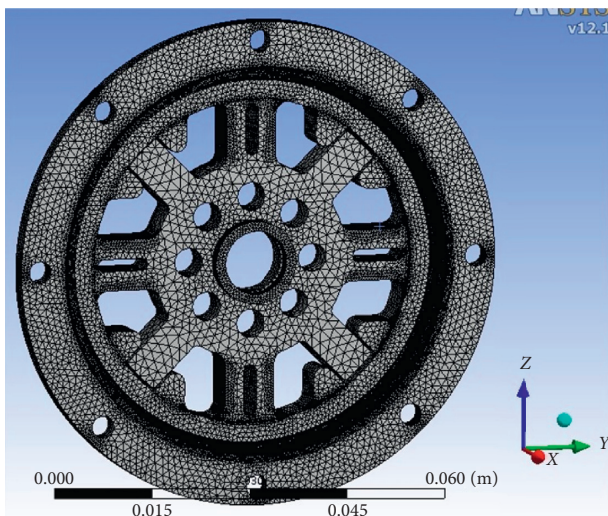


FIGURE 3: Axis of the torque sensor for FEM analysis.

TABLE 1: Design parameters of the torque sensor by FEM.

Quantity	Length (mm)	Width (mm)	Height (mm)
Spoke	10	12	6
Slit	8	1.6	6

communication protocol. The microcontroller can directly collect the temperature signal by its ADC. The schematic diagram of the sensor circuit is shown in Figure 5, and the developed torque sensor is displayed in Figure 6.

2.3. Torque Ripple Cancellation. As shown in Figure 7(a), for each revolution of the elliptical wave generator of the harmonic drive, the flexspline produces two cycles of deformation, resulting in the torque ripple depicted by curve A in Figure 7(b). As shown in Figure 7(b), the periodic interference can be eliminated by adding the torque ripple curve A to the other curve \bar{A} with the same amplitude and frequency but with phase difference of $\pi/2$.

To cancel the torque ripple, four strain gauges $R_1 - R_4$ are mounted on the optimum location at both sides of the spoke to collect the strain signals (Figure 8(a)) and form the Wheatstone bridge (Figure 8(b)). The theoretical analysis is as follows.

When a clockwise torque T is applied to the sensor, the odd-numbered strain gauges are under tension, while the even-numbered strain gauges are under compression. Strains ϵ_1 and ϵ_2 measured by gauges R_1 and R_2 , respectively, can be expressed as follows:

$$\begin{cases} \epsilon_1 = \epsilon_t + \epsilon_w, \\ \epsilon_2 = -\epsilon_t + \epsilon_w, \end{cases} \quad (1)$$

where ϵ_t is the tensile strain caused by the applied torque and ϵ_w is the tensile strain due to the deformation of the flexspline. To obtain the information of ϵ_t , the difference between strains ϵ_1 and ϵ_2 is written as follows:

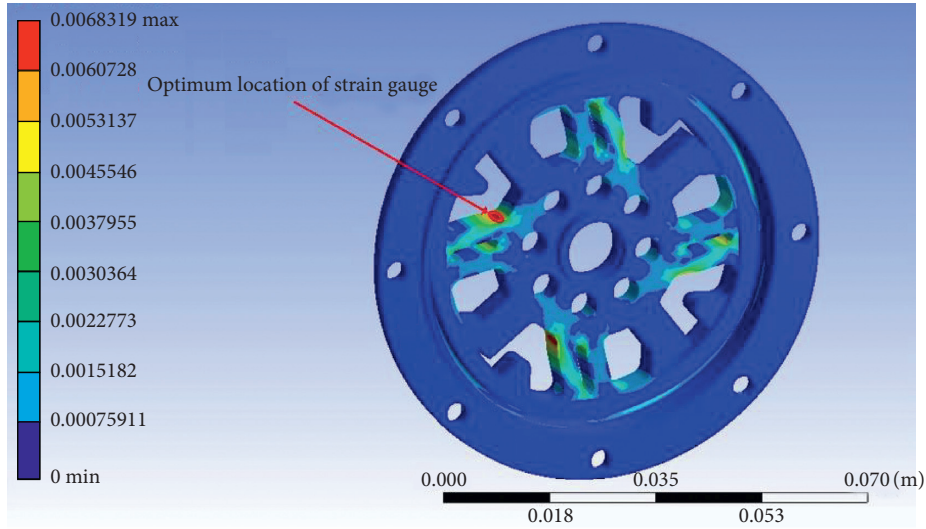


FIGURE 4: Deformation behavior of the torque sensor.

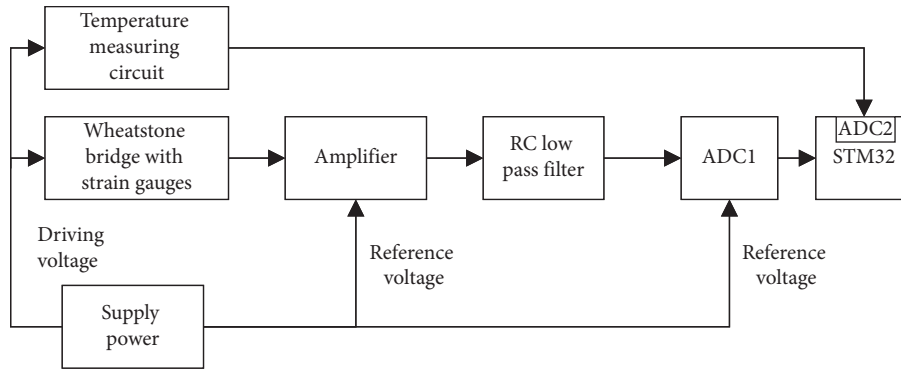


FIGURE 5: Schematic circuit diagram of sensor.

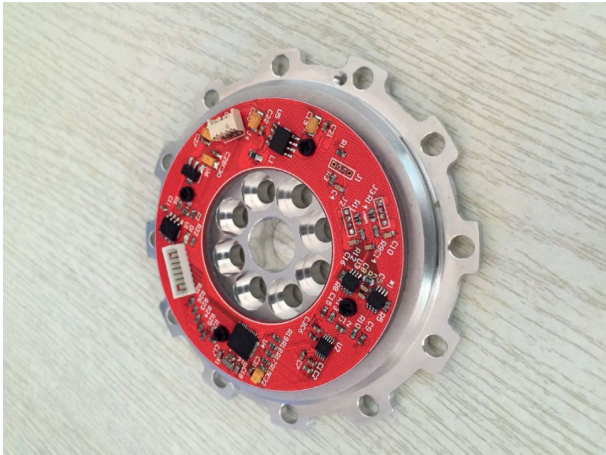


FIGURE 6: Developed torque sensor.

$$\varepsilon_1 - \varepsilon_2 = 2\varepsilon_t + \Psi_0 \sin(2\beta), \quad (2)$$

where the difference $\varepsilon_\omega - \varepsilon_{\omega'}$ is assumed to be sinusoidal as explained by Hashimoto [12] and β is the rotational angle of the wave generator to the reference point.

To measure strain ε_t and eliminate $\Psi_0 \sin(2\beta)$, another signal \bar{A} as mentioned above should be obtained. Gauges R_3 and R_4 are on the spoke rotating at 90° from the position of R_1 and R_2 . Signal \bar{A} can be obtained by the difference of strain ε_3 and ε_4 , which are measured by gauges R_3 and R_4 , respectively.

$$\varepsilon_3 - \varepsilon_4 = 2\varepsilon_t + \Psi_0 \sin(2\beta - \pi). \quad (3)$$

Equations (2) and (3) can be added to cancel the sinusoid component as follows:

$$\varepsilon_1 - \varepsilon_2 + \varepsilon_3 - \varepsilon_4 = 4\varepsilon_t. \quad (4)$$

Thus, the Wheatstone bridge composed of R_1 , R_2 , R_3 , and R_4 can generate a voltage signal proportional to strain ε_t .

$$U_o = \left(\frac{K}{4}\right)(\varepsilon_1 + \varepsilon_3 - \varepsilon_2 - \varepsilon_4)U_i = K\varepsilon_t U_i, \quad (5)$$

where K is the strain coefficient of the gauges, and U_i and U_o represent the input and output voltages of the Wheatstone bridge.

If the bridge is subject to the same change in temperature, the strain due to temperature is canceled out. To minimize the sticking error and enhance the temperature

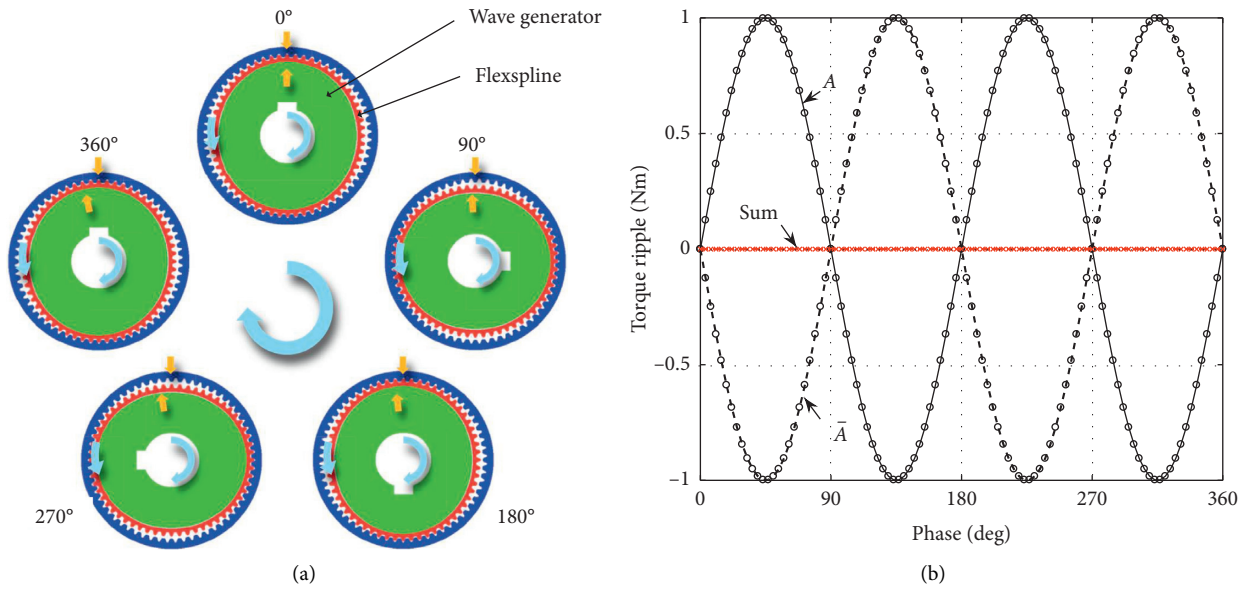


FIGURE 7: Relationship between the rotation of the wave generator and torque ripple: (a) deformation of the flexspline and (b) elimination of the torque ripple.

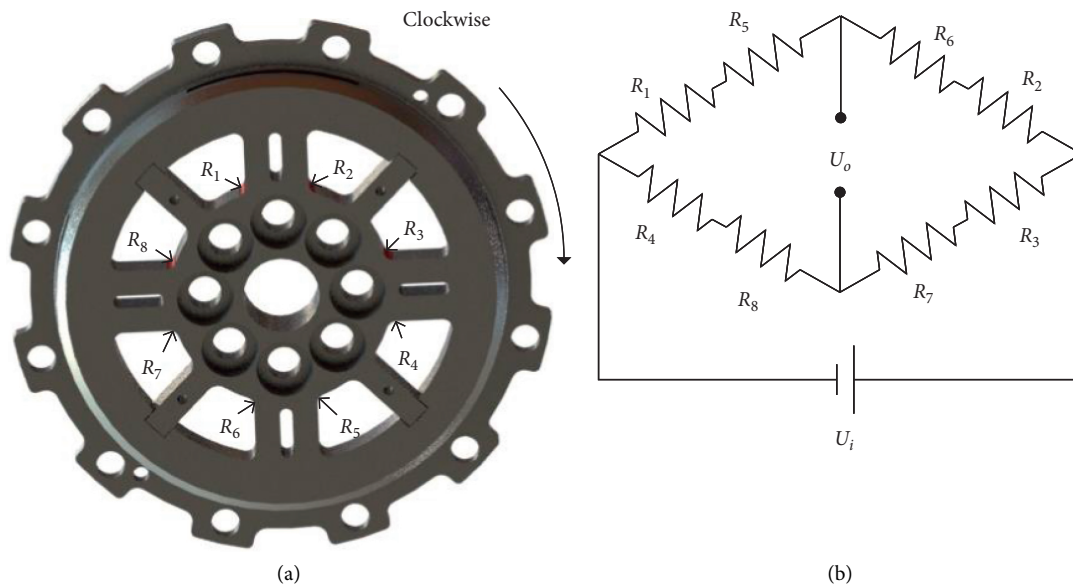


FIGURE 8: Sticking position of the strain gauge and the Wheatstone bridge circuit for joint torque sensing: (a) configuration of the strain gauges and the (b) Wheatstone bridge.

compensation, another four strain gauges, $R_5 - R_8$, are introduced to maintain the symmetry with $R_1 - R_4$, as shown in Figures 8(a) and 8(b). In this study, the sticking process of the strain gauges is carried out under a microscope with the scale display, minimizing the error caused by sticking the strain gauges.

2.4. Temperature Compensation Method. The Wheatstone bridge circuit, which is composed of eight strain gauges, can eliminate theoretically the effect of temperature. However, due to the distinct change in temperature of

each strain gauge, accurate torque information is difficult to obtain if only the circuit is used. Therefore, on the basis of hardware compensation, this study adopts software to compensate for the temperature drift. The specific method is to measure the elastic body temperature with a built-in thermistor. Then, the experimental data are obtained to solve the temperature compensation model based on the least square method.

The change in the temperature of the sensor can be measured by the thermistor pasted on the body of the sensor. The temperature-measuring circuit and the pasting position of the thermistor are shown in Figure 9.

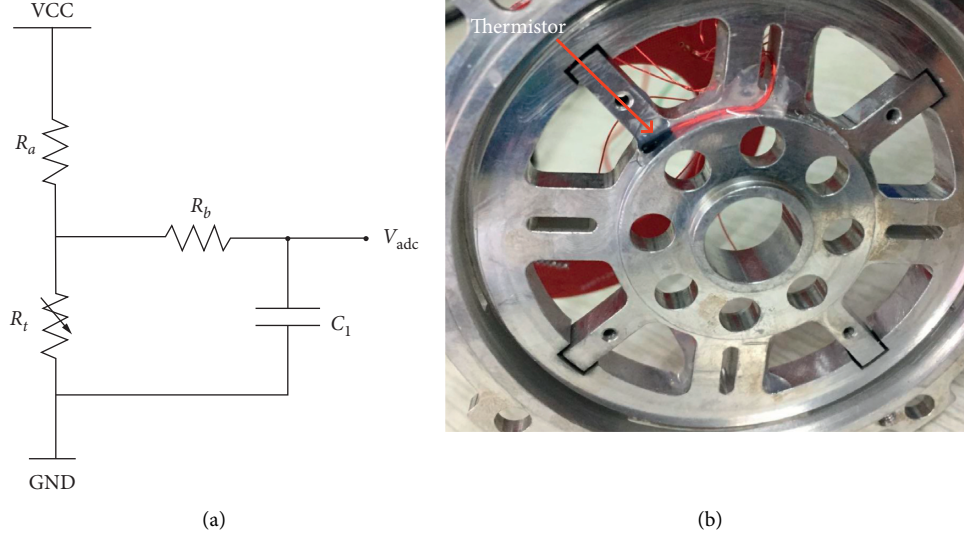


FIGURE 9: Temperature-measuring method: (a) thermistor measuring circuit and (b) pasting position of the thermistor.

According to Figure 9(a), the resistance of the thermistor can be calculated as follows:

$$R_t = \frac{V_{\text{adc}} R_a}{V_{\text{CC}} - V_{\text{adc}}}, \quad (6)$$

where R_a is the voltage divider; R_t is the thermistor; R_b and C_1 constitute the RC low pass filter circuit; and V_{adc} is the input voltage of the analog-to-digital converter.

In addition, the temperature of the thermistor related to the resistance of thermistor can be expressed as follows:

$$T_t = \frac{BT_{\text{nom}}}{T_{\text{nom}}(\ln R_t - \ln R_{\text{nom}}) + B}, \quad (7)$$

where R_{nom} is the nominal resistance of the thermistor at 25°C ; B is the known parameter of the thermistor; T_{nom} is the Kelvin temperature corresponding to 25°C ; and T_t is the measurement temperature described by the Kelvin temperature. Substituting R_t as given in (6) into (7), the current temperature of the sensor can be easily calculated.

The applied torque of the sensor related to the output voltage of the Wheatstone bridge can be expressed as follows:

$$\tau = kV + b, \quad (8)$$

where k is the sensor sensitivity independent of temperature and b is the temperature drift that can be modeled as a second-degree polynomial related to temperature T as follows:

$$b = A_0 + A_1T + A_2T^2. \quad (9)$$

Substituting (9) into (8), the output of the sensor can be presented as follows:

$$\tau = kV + A_0 + A_1T + A_2T^2. \quad (10)$$

When the applied torque of the sensor is 0, the temperature drift model of the sensor can be obtained as follows:

$$V = -\left(\frac{A_0}{k}\right) - \left(\frac{A_1T}{k}\right) - \left(\frac{A_2T^2}{k}\right) = A'_0 + A'_1T + A'_2T^2. \quad (11)$$

To acquire an accurate torque information, parameters A'_0 , A'_1 , and A'_2 should be estimated. In this study, polynomial fitting is used to solve the parameters by using at least three sets of experimental data.

2.5. Collision Detection Method. To reflect the comprehensive performance of the joint torque sensor, the proposed torque sensor is applied to the collision detection, which is one of the most typical applications of a collaborative robot. The schematic diagram of collision detection is shown in Figure 10.

The dynamic of a robot system with n degrees of freedom can be modeled as follows:

$$\tau_m + \tau_c - \tau_f = M(\theta)\ddot{\theta} + C(\theta, \dot{\theta})\dot{\theta} + g(\theta), \quad (12)$$

where θ , $\dot{\theta}$, and $\ddot{\theta} \in R^n$ are the vectors of the generalized joint coordinates, velocities, and acceleration, respectively; $M(\theta) \in R^{n \times n}$ is the joint-space inertia matrix; $C(\theta, \dot{\theta}) \in R^{n \times n}$ is the Coriolis and centripetal coupling matrix; $G(\theta) \in R^n$ is the gravity loading; $\tau_f \in R^n$ is the friction force; $\tau_m \in R^n$ is the vector of generalized actuator force associated with the generalized coordinate θ ; and $\tau_c \in R^n$ is the joint force due to the external torque.

Based on the robot dynamic characteristic that $\dot{M}(\theta) - 2C(\theta, \dot{\theta})$ is a skew symmetric matrix, the following equation is obtained:

$$\dot{M}(\theta) = C(\theta, \dot{\theta}) + C^T(\theta, \dot{\theta}). \quad (13)$$

To estimate the external torque, the generalized momentum of robot is modeled as follows:

$$p = M(\theta)\dot{\theta}. \quad (14)$$

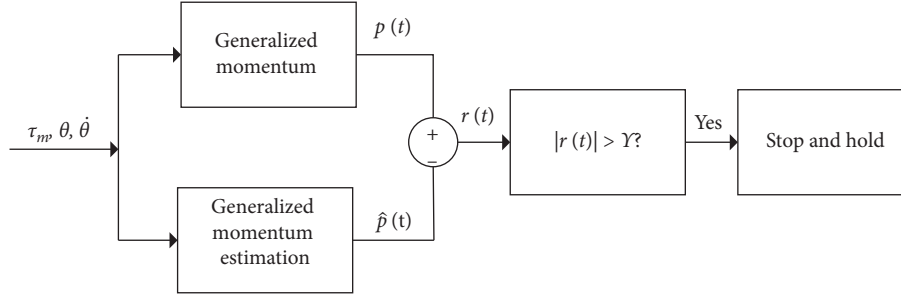


FIGURE 10: Schematic diagram of collision detection.

Given the time derivative of p ,

$$\dot{p} = M(\theta)\ddot{\theta} + C^T(\theta, \dot{\theta})\dot{\theta} + C(\theta, \dot{\theta})\dot{\theta}, \quad (15)$$

and substituting (15) into (12) yields

$$\tau_c = -\tau_m + \dot{p} - C^T(\theta, \dot{\theta})\dot{\theta} + g(\theta) + \tau_f. \quad (16)$$

The observer about joint force τ_c can be designed as follows:

$$\dot{r} = K_O(\tau_c - r), \quad (17)$$

where $K_O = \text{diag}(k_{o,i}) > 0$ is a diagonal gain matrix. Substituting (16) into (17) and then integrating (17), the observer $r(t)$ with initial condition $r(0) = 0$ can be expressed as follows:

$$r(t) = K_O \left[p(t) - \int_0^t (\tau_m + C^T(\theta, \dot{\theta})\dot{\theta} - g(\theta) - \tau_f + r) du - p(0) \right]. \quad (18)$$

The Laplace transform of (17) can be expressed as follows:

$$r(s) = \frac{K_O}{K_O + s} \tau_c(s). \quad (19)$$

Equation (19) is a first-order low pass filter. Hence,

$$K_O \longrightarrow \infty \Rightarrow r \approx \tau_c. \quad (20)$$

One of the basic characteristics of the first-order low pass filter is that high-frequency noise signal will not pass, and a greater value of K_O can obtain a faster step response. This good characteristic makes the generalized momentum observer a good virtual force sensor, which is used to measure the external force acting on the robot.

Given the errors of dynamic modeling and friction identification, $r(t)$ cannot be accurately calculated. Thus, the estimation $\hat{r}(t)$ is used in this experiment [18].

$$\hat{r}(t) = K_O \left[\hat{p}(t) - \int_0^t (\hat{\tau}_m + \hat{C}^T(\theta, \dot{\theta})\dot{\theta} - \hat{\tau}_f - \hat{g}(\theta) + \hat{r}) du - \hat{p}(0) \right], \quad (21)$$

where $\hat{p}(t)$ is the estimated robot-generalized momentum at time $t \geq 0$; $\hat{\tau}_m$ is the measured torque; $\hat{\tau}_f$ is the friction torque; the matrix $\hat{C}^T(\theta, \dot{\theta})$ comprises the Coriolis and centrifugal terms; and $\hat{g}(\theta)$ is the gravity vector.

The collision of a robot is detected by the observer algorithm by setting the collision detection threshold as follows:

$$|\hat{r}(t)| > \Upsilon, \quad (22)$$

where $\Upsilon \in R^n$ is the vector of the collision detection threshold. In practical application, the threshold cannot be too small. Otherwise, misjudgment will occur. If the threshold is too high, the robot becomes less sensitive to collision. The threshold is minimized as error and noise are considered.

3. Experimental Setups

3.1. Calibration Setup. The dynamic calibration of the joint torque sensor is performed on the developed automatic calibration system, which includes a dynamic calibration platform and an application program based on LabVIEW. As shown in Figure 11, the dynamic calibration platform involves a magnetic powder brake, a slip-ring, a reference sensor (TS11-200-B, INTERFACE), the developed sensor, the developed modular joint, a potentiometer, a data acquisition device, an amplifier, a power supply, and a connecting part. The developed sensor is connected to the reference sensor by the connecting part. The application program collects the torque signal of the reference sensor through the data acquisition device and the output voltage signal and temperature signal of the developed sensor via RS485. Thus, the real-time drawing function of the signals is realized.

During calibration, the modular joint moves at a constant speed, and the brake force of the magnetic powder brake is controlled by adjusting the output voltage of the potentiometer to obtain the desired applied torque read from the reference torque. In this setup, a torque interval from 0 Nm to 70 Nm is applied, which is equal to the peak torque of the motor magnified by the harmonic drive.

3.2. Collision Detection Setup. An experiment system is used to examine the collision detection method (Figure 12). The system consists of the developed modular joint, the developed torque sensor, a motor driver (Golo Solo Whistle series, Elmo), a motor controller (Platinum Maestro, Elmo), and a one-link arm. The dynamics of the arm can be modeled as follows.

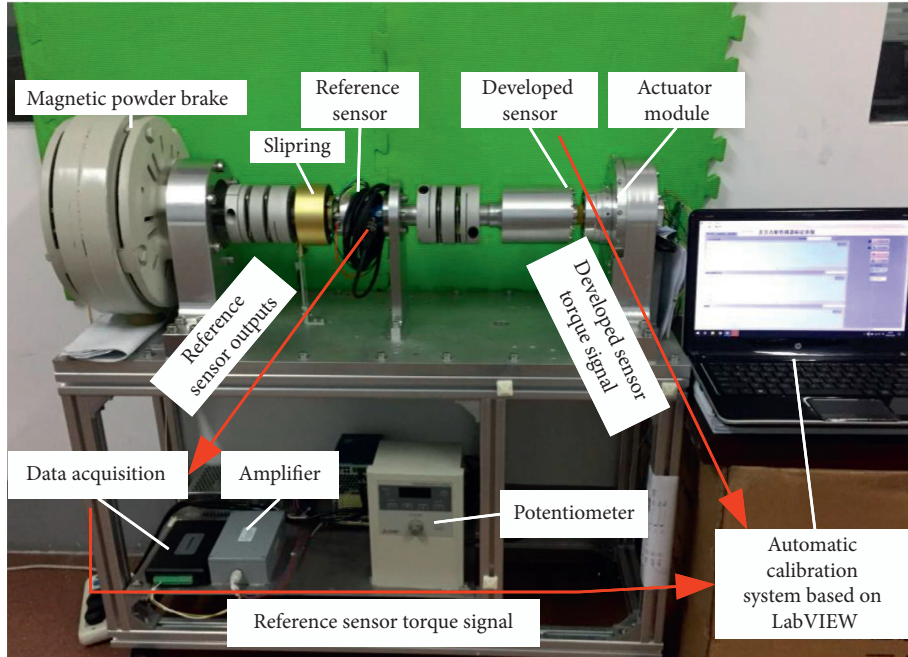


FIGURE 11: Developed dynamic calibration system.

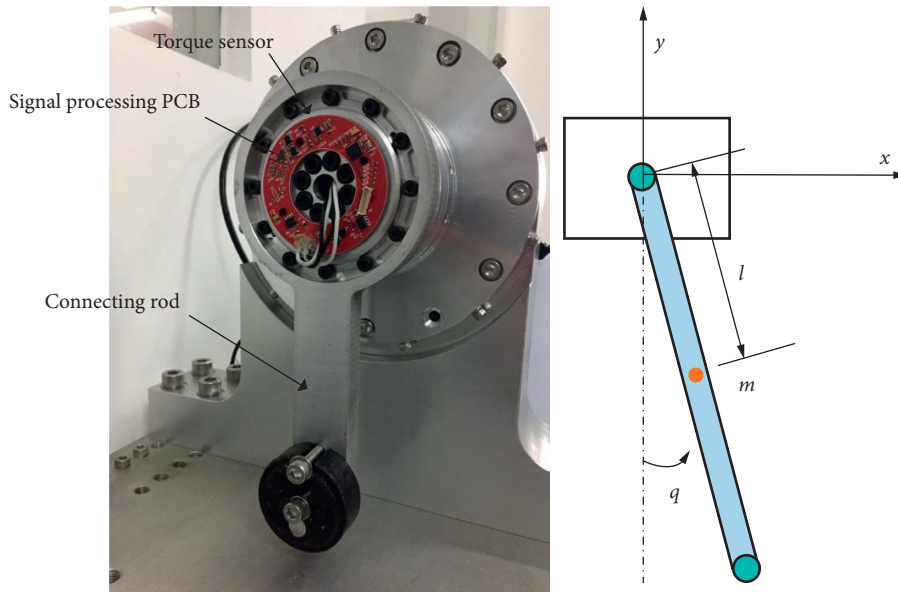


FIGURE 12: Experiment setup for collision detection.

$$\tau = (ml^2 + J)\ddot{q} + mgl \sin(q), \quad (23)$$

where q and \ddot{q} represent the arm angle and acceleration, respectively; m is the arm quality; l is the distance from the center of mass to the axis of the joint; J is the arm inertial; and τ is the measured torque from the torque sensor. The identified parameters of the dynamic model are listed in Table 2.

4. Results and Discussion

4.1. Evaluation of the Torque Ripple Cancellation. Two of the developed sensors are needed to verify the effectiveness of the torque ripple cancellation method. One sensor adopts the

TABLE 2: Parameters of the one-link arm.

$ml^2 + J$ (kg · m ²)	mgl (Nm)
0.0096	0.5022

strain gauge configuration as shown in Figure 13, while the other sensor adopts the strain gauge configuration as shown in Figure 8. The former is the type without torque ripple cancellation, and the latter has torque ripple cancellation. The modular joint is equipped with these two sensors. Then, the modular joint is rotated at a velocity of 35.16°/s without load. The sensor outputs of these two configurations are collected



FIGURE 13: Common strain gauge configuration.

separately, and then fast Fourier transform (FFT) is conducted.

Figure 14(a) shows that the voltage curve representing the torque ripple is fluctuating. Figure 14(b) demonstrates that the curve of the torque ripple becomes flatter, and its amplitude is almost equal to the temperature drift. In addition, Figure 15 shows the FFT plot of both torque signals. Figure 15(a) shows two peaks at 19.76 Hz and at 9.89 Hz, which correspond to the torque ripple. Figure 15(b) displays the FFT plot of the signal with the torque ripple cancelation. No peaks are observed at 19.76 Hz and 9.89 Hz. Therefore, the torque ripple is clearly reduced. This method does not need any additional software filtering algorithm and will not cause delay of the torque signal.

4.2. Evaluation of Temperature Compensation. The temperature drift of the sensor is caused by the increase in temperature rather than a drop in temperature [16]. Therefore, in this paper, the hysteresis of the temperature drift is ignored, and only the case of temperature rise is considered. To verify the temperature compensation method, the temperature of the sensor is between 20°C and 45°C with an increment of 5°C. Thus, the output of the sensor varies with the change in temperature. The output data are collected to fit the temperature compensation model by using the method described in Section 2.4. Figure 16 displays the relationship between the temperature and the output voltage of the sensor. The measured temperature and the voltage showed a nonlinear relationship. In this study, a second-degree polynomial curve is applied to fit the nonlinear curve. The fit equation can be expressed as follows:

$$b(T) = 0.0102T^2 - 0.8704T - 21.39. \quad (24)$$

To evaluate the effectiveness of the temperature compensation method, the sensor output before and after the compensation is collected and compared. As shown in

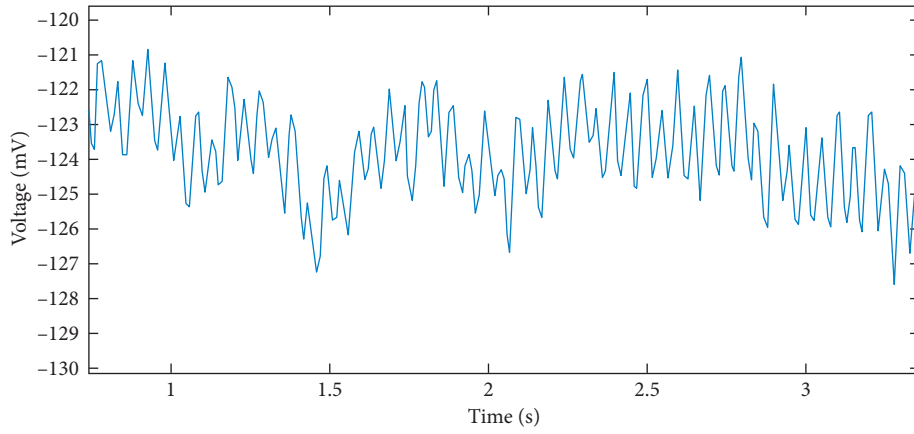
Figure 17, the output torque of the sensor increases with temperature before the compensation, and the maximum value is 0.38 Nm. After the compensation, the output torque decreases apparently, and the maximum error is 0.08 Nm.

4.3. Calibration. During calibration, the modular joint moves at 2°/s in a counterclockwise direction, and the brake force of the magnetic powder brake is controlled to apply the desired torque that ranges between 0 Nm and 70 Nm with an increment of 5 Nm on the reference and developed sensors. The output data are collected from the reference and developed sensors, respectively. As shown in Figure 18, the x -axis corresponds to the voltage data from the developed sensor, and the y -axis corresponds to the applied torque measured by the reference torque sensor. The measured voltage and the applied torque show a linear relationship. In this study, a first-degree polynomial curve is applied to fit the linear curve. The fit equation can be expressed as follows:

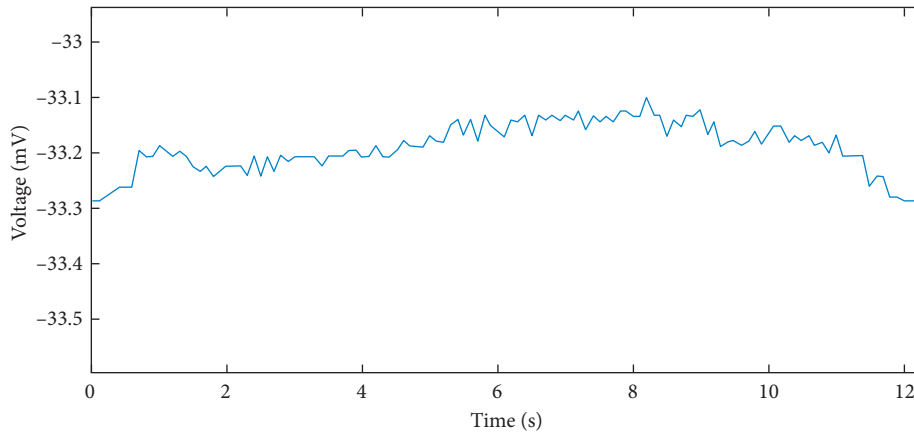
$$\tau = 62.738x + 2.1835. \quad (25)$$

Therefore, the nonlinear error of the torque sensor is 0.878%, and the hysteresis is 0.903%. The sensitivity is $0.0627 \text{ Nm} \cdot (\text{mV})^{-1}$, and the temperature drift is -34.8 mV . The performance of the developed torque sensor is compared with that of the commercialized torque sensor M2210C1 (Sunrise Instruments). The comparative results are provided in Table 3. M2210C1 shows better performance than the developed sensor. However, because the output signal of M2210C1 is an analog signal, high-frequency noise can be mixed with this signal. In addition, the developed sensor is lighter than M2210C1 and can be calibrated online with the modular joint to improve sensing accuracy.

4.4. Evaluation of Collision Detection. To verify intuitively the effectiveness of the collision detection method described in Section 2.5, the experimental setup shown in Figure 19 is adopted. An egg is erected between the one-link arm and the

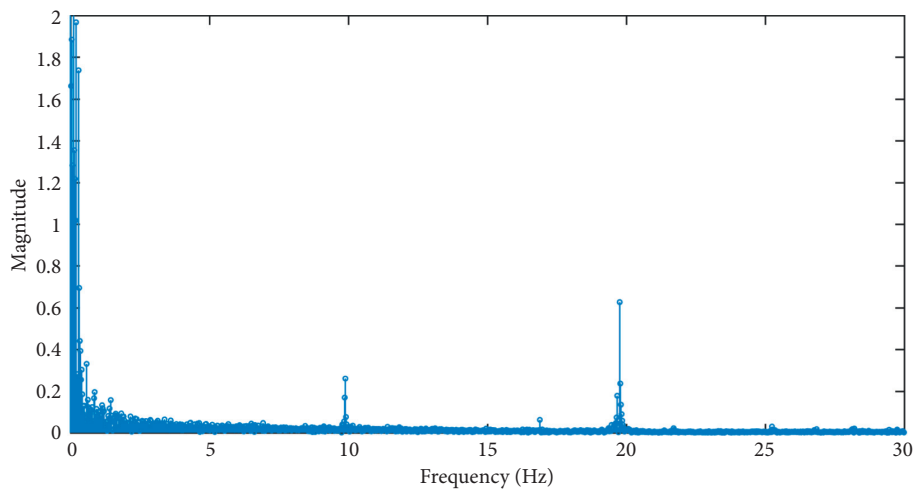


(a)



(b)

FIGURE 14: Experimental result of the modular joint at a constant velocity (a) before and (b) after torque ripple compensation.



(a)

FIGURE 15: Continued.

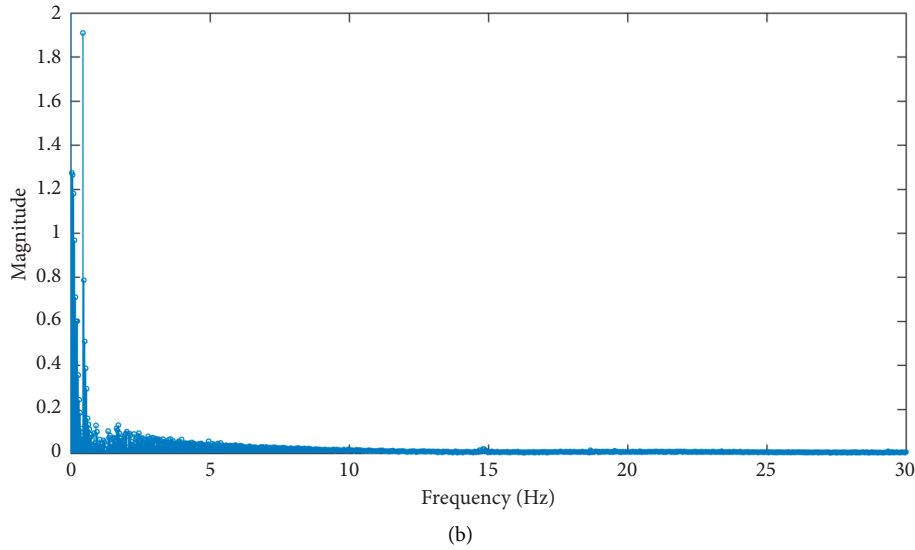


FIGURE 15: Fast Fourier transformation (FFT) results: FFT plots (a) without and (b) with torque ripple compensation.

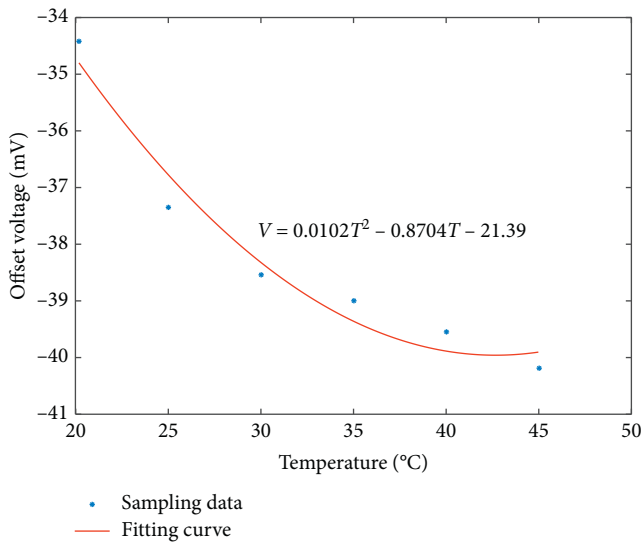


FIGURE 16: Temperature drift fitting.

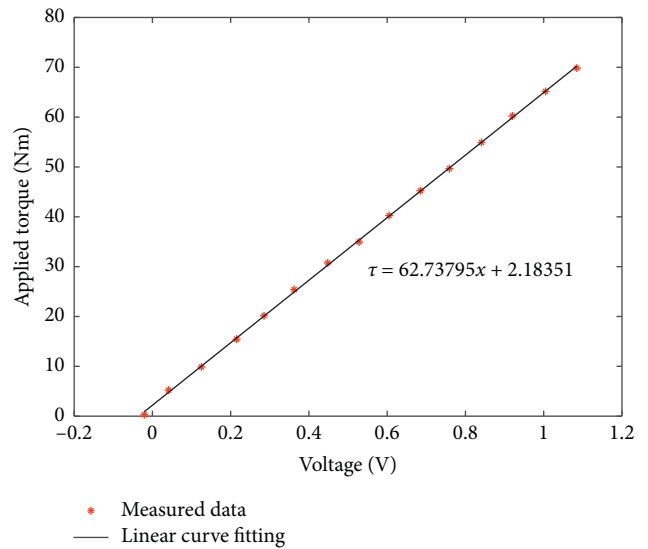


FIGURE 18: Measured torque and fitting process.

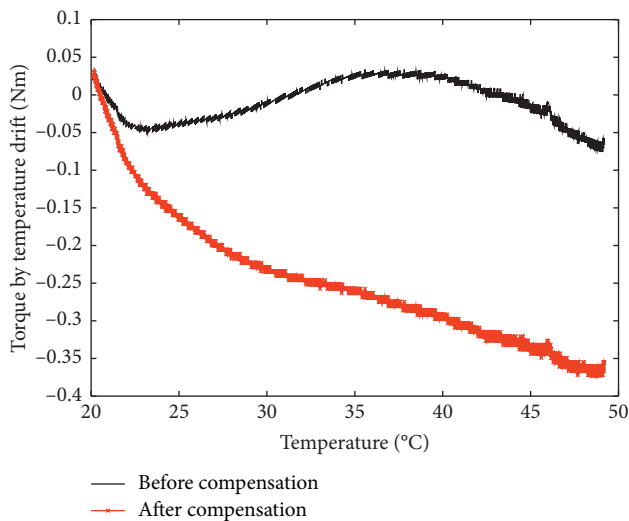


FIGURE 17: Evaluation of the temperature drift compensation.

obstacle. Then, the arm is controlled to collide horizontally with the egg. The obstacle limits the displacement of the egg after impact. When the impact torque is detected, the movement of the arm stops. In this experiment, the identified dynamic parameters (Table 2) of the arm are used for the observer of the external force, and the observer gain coefficient K_o is equal to 100. The speed signal is filtered, and the sampling frequency is set to 100 Hz. To set a reasonable collision detection threshold, the arm moves in different directions at distinct speeds without an external force acting on it. The estimated torque of the observer satisfies $|\hat{r}(0)| < 0.0255$ Nm. Thus, the collision detection threshold is set to 0.03 Nm.

The movement velocity of the arm is between $30^\circ(\text{s})$ and $60^\circ(\text{s})$. Figure 20 displays the estimated impact torque with no broken egg. These phenomena show that the designed joint torque sensor can effectively detect collision with short delay.

TABLE 3: Performance of the commercial and developed torque sensors.

Quantity	Height (mm)	Diameter (mm)	Weight (g)	Sensing range (Nm)	Nonlinearity (%)	Hysteresis (%)	Output type
M2210C1	7	80	180	100	0.5	1	Analog
Developed sensor	10	86	60.6	70	0.878	0.903	Digital



FIGURE 19: Experimental setup for the collision detection with egg.

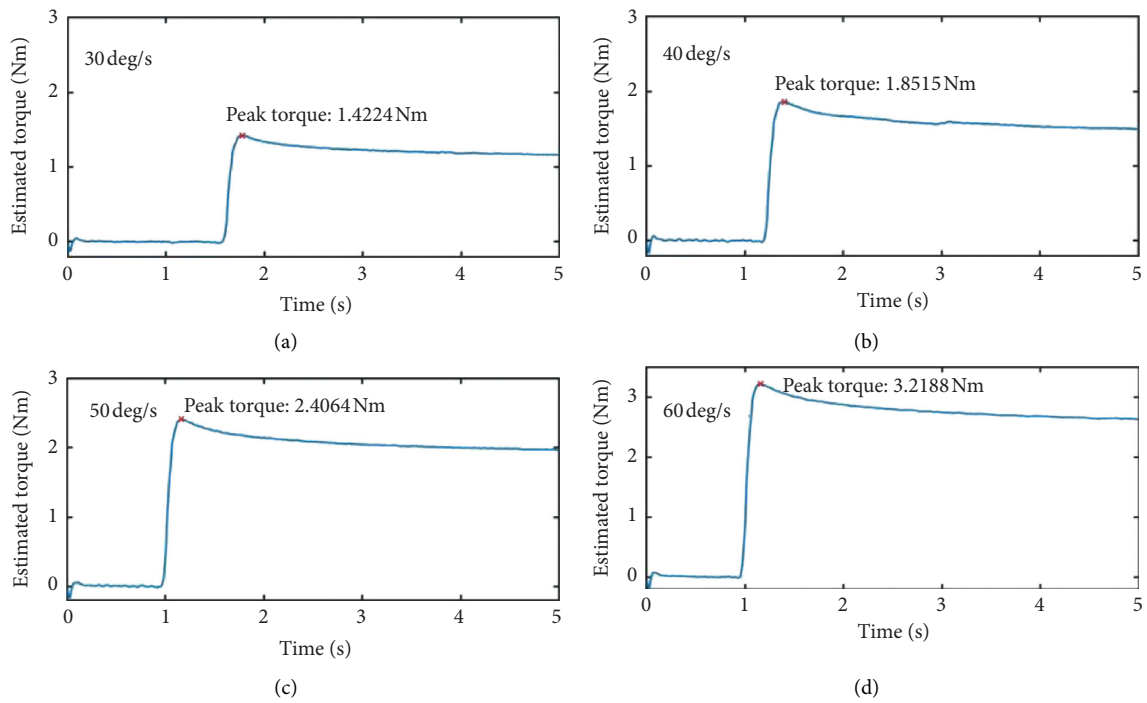


FIGURE 20: Collision torque detection.

5. Conclusion and Future Work

In this paper, a torque sensor sensing technique is introduced for the developed modular joint. Based on theoretical and experimental research, the torque ripple is clearly reduced by using a spoke-type sensor body and a special strain gauge configuration. In addition, the temperature drift is compensated by using the combination of the Wheatstone bridge and the proposed temperature drift model.

The performance of the developed torque sensor is compared with that of a commercial sensor. The commercial torque sensor, namely, M2210C1, shows better resolution in its torque-sensing ability. However, the output voltage of this sensor is an analog signal, and, compared with the digital output, electromagnetic noise can be easily introduced to the analog signal. In addition, the developed sensor is lighter than M2210C1 and can be calibrated online with the modular joint to overcome the sensing error caused by assembly. Furthermore, the developed modular joint and the proposed torque sensor show good collision detection performance.

In this study, only a modular joint is employed to assess the torque ripple cancelation and the temperature drift compensation. A collaborative robot with multiple degrees of freedom will be evaluated in future studies.

Data Availability

As the project will not be finished until May 2022 and we have confidentiality agreement with the State Key Laboratory of Robotics and System, the data could not be released so far. For any information about the article, please contact us via zhanghe0451@hit.edu.cn.

Conflicts of Interest

The authors declare that there are no conflicts of interest regarding the publication of this paper.

Acknowledgments

This work was supported by the National Key R&D Program of China (Grant no. 2018YFB1307602), open foundation of the State Key Laboratory of Robotics and Systems (Harbin Institute of Technology) (Grant no. SKLRS201816B), Major Research Plan of the National Natural Science Foundation of China (Grant no. 91648201), and Foundation for Innovation Research Groups (Grant no. 51521003) of the National Natural Science Foundation of China.

References

- [1] U. Kim, Y. B. Kim, D.-Y. Seok, J. So, and H. R. Choi, "A surgical palpation probe with 6-axis force/torque sensing capability for minimally invasive surgery," *IEEE Transactions on Industrial Electronics*, vol. 65, no. 3, pp. 2755–2765, 2018.
- [2] Y. Park, S. C. Ryu, R. J. Black et al., "Exoskeletal force-sensing end-effectors with embedded optical fiber-bragg-grating sensors," *IEEE Transactions on Robotics*, vol. 25, no. 6, pp. 1319–1331, 2009.
- [3] A. Mohammed, B. Schmidt, and L. Wang, "Active collision avoidance for human-robot collaboration driven by vision sensors," *International Journal of Computer Integrated Manufacturing*, vol. 30, no. 9, pp. 970–980, 2017.
- [4] S. D. Lee, M. C. Kim, and J.-B. Song, "Sensorless collision detection for safe human-robot collaboration," in *Proceedings of the 2015 IEEE/RSJ International Conference on Intelligent Robots and Systems (IROS)*, pp. 2392–2397, Hamburg, Germany, 2015.
- [5] R. P. Ubeda, S. C. Gutiérrez Rubert, R. Z. Stanisci, and Á. P. Ivars, "Design and manufacturing of an ultra-low-cost custom torque sensor for robotics," *Sensors*, vol. 18, no. 6, p. 1786, 2018.
- [6] Y. B. Kim, U. Kim, D.-Y. Seok, J. So, Y. H. Lee, and H. R. Choi, "Torque sensor embedded actuator module for robotic applications," *IEEE/ASME Transactions on Mechatronics*, vol. 23, no. 4, pp. 1662–1672, 2018.
- [7] Y. Kuroki, Y. Kosaka, T. Takahashi et al., "Cr-N alloy thin-film based torque sensors and joint torque servo systems for compliant robot control," in *Proceedings of the 2013 IEEE International Conference on Robotics and Automation*, pp. 4954–4959, Karlsruhe, Germany, May 2013.
- [8] S. Lee, K. Yang, E. Shin, and H. Kim, "Development of 1-axis torque sensor with different shape of support and measurement spoke," in *Proceedings of the 2014 11th International Conference on Ubiquitous Robots and Ambient Intelligence (URAI)*, pp. 688–691, Kuala Lumpur, Malaysia, November 2014.
- [9] B.-J. Jung, B. Kim, J. C. Koo, H. R. Choi, and H. Moon, "Joint torque sensor embedded in harmonic drive using order tracking method for robotic application," *IEEE/ASME Transactions on Mechatronics*, vol. 22, no. 4, pp. 1594–1599, 2017.
- [10] H. D. Taghirad and P. R. Belanger, "Intelligent built-in torque sensor for harmonic drive systems," *IEEE Transactions on Instrumentation and Measurement*, vol. 48, no. 6, pp. 1201–1207, 1999.
- [11] B.-J. Jung, B. C. Kim, S. Kim, J. C. Koo, H. R. Choi, and H. Moon, "Torque ripple compensation method for joint torque sensor embedded in harmonic drive using order analysis," in *Proceedings of the Sensors, 2014 IEEE*, pp. 1932–1935, Valencia, Spain, November 2014.
- [12] M. Hashimoto, Y. Kiyosawa, and R. P. Paul, "A torque sensing technique for robots with harmonic drives," *IEEE Transactions on Robotics and Automation*, vol. 9, no. 1, pp. 108–116, 1993.
- [13] I.-M. Kim, H.-S. Kim, and J.-B. Song, "Embedded joint torque sensor with reduced torque ripple of harmonic drive," in *Intelligent Autonomous Systems 12*, pp. 633–640, Springer, Berlin, Heidelberg, 2013.
- [14] N. Kashiri, J. Malzahn, and N. G. Tsagarakis, "On the sensor design of torque controlled actuators: a comparison study of strain gauge and encoder-based principles," *IEEE Robotics and Automation Letters*, vol. 2, no. 2, pp. 1186–1194, 2017.
- [15] S. Y. Choi, T. K. Kim, D. Y. Kim, B. S. Kim, J. H. Hwang, and C. W. Park, "Development of joint torque sensor applied to compensate crosstalk error," in *Proceedings of the 2012 IEEE International Conference on Automation Science and Engineering (CASE)*, pp. 1086–1088, Seoul, Republic of Korea, August 2012.
- [16] F. J. A. Chavez, G. Nava, S. Traversaro, F. Nori, and D. Pucci, "Model based in situ calibration with temperature compensation of 6 axis force torque sensors," in *Proceedings of the*

- 2019 International Conference on Robotics and Automation (ICRA)*, pp. 5397–5403, Montreal, QC, Canada, May 2019.
- [17] Y. Sun, Y. Liu, and H. Liu, “Temperature compensation for six-dimension force/torque sensor based on radial basis function neural network,” in *Proceedings of the 2014 IEEE International Conference on Information and Automation (ICIA)*, pp. 789–794, Hailar, China, July 2014.
- [18] A. De Luca, A. Albu-Schaffer, S. Haddadin, and G. Hirzinger, “Collision detection and safe reaction with the DLR-III lightweight manipulator arm,” in *Proceedings of the 2006 IEEE/RSJ International Conference on Intelligent Robots and Systems*, pp. 1623–1630, Beijing, China, October 2006.